Nanoscale Imaging and Control of hexagonal Boron-Nitride Single Photon Emitters by a Resonant Nano-antenna

Nicola Palombo Blascetta[1], Matz Liebel[1], Xiaobo Lu[1],
T. Taniguchi [2], K. Watanabe[2], Dmitri K. Efetov[1] and Niek F. van Hulst[1,3]

[1]ICFO, Institut de Ciences Fotoniques, The Barcelona Institute of Science and Technology, Castelldefels, Barcelona 08860, Spain

[2]National Institute for Materials Science, 1-1 Namiki, Tsukuba, Ibaraki 305-0044, Japan

[3]ICREA, Institució Catalana de Recerca i Estudis Avançats, Barcelona 08010, Spain

Abstract: Defect centers in two-dimensional hexagonal boron-nitride (hBN) are drawing attention as single-photon emitters with high photo-stability at room temperature. With their ultra-high photon-stability, hBN single-photon emitters are promising for new applications in quantum technologies and for 2D-material based optoelectronics. Here, we control the emission rate of hBN-defects by coupling to resonant plasmonic nanocavities. By deterministic control of the antenna we acquire high-resolution emission maps of the single hBN-defects. Using time-gating, we can discriminate the hBN-defect emission from the antenna luminescence. We observe sharp dips (40 nm FWHM) in emission, together with a reduction in luminescence lifetime. Comparing with FDTD simulations we conclude that both radiative and non-radiative rates are enhanced, effectively reducing the quantum efficiency. Also, the large refractive index of hBN largely screens off the local antenna field enhancement. Finally, based on the insight gained, we propose a close-contact design for an order of magnitude brighter hBN single-photon emission.

Keywords: hBN-defect center; single-photon source; dipole antenna; nanoantenna; scanning probe; superresolution; enhancement; quenching; luminescence lifetime.

TOC Figure

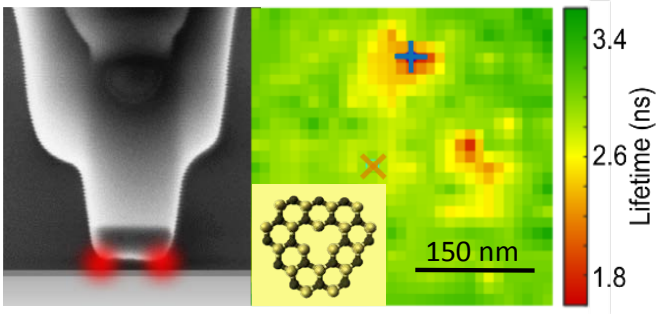

Bright and stable single-photon sources are highly on demand for emerging quantum technologies, such as quantum computing[1] or encryption schemes[2], where non-classical light sources are required, to provide on-demand indistinguishable photons, one at a time. To this end, quantum dots (QD)[3], organic molecules in crystalline matrices[4,5], diamond nitrogen and silicon vacancy centers[6,7], and 2D transition metal dichalcogenides (TMDC)[8] are all actively explored. Recent progress in efficient coupling of single molecules[5], NV centers[9] or QDs[10] to waveguides is paving the way to top-down fabricated single-photon sources on-chip.

However, the applications of single-photon emitters face intrinsic limits. The achievable brightness is limited by the luminescence lifetime and intermediate dark states. Molecules tend to bleach, while both molecules and QDs tend to blink. The blinking and bleaching can be alleviated by embedding the molecules in a suitable crystalline matrix[11], or encapsulating the QDs in an engineered higher bandgap shell. Notably, the brightness can be boosted by enhancing the radiative rate (reducing the lifetime) with an engineered plasmonic antenna at nanometer distance[12,13]. Unfortunately, the necessary thickness of the protecting shell for photostability, such as the crystalline matrix around molecules or the diamond surrounding the NV center, does prevent the close proximity of plasmonic antennas.

Recently, the hexagonal boron nitride (hBN) atomic defect is attracting major attention as an alternative candidate for a high-performance single-photon source[14,15]. The hBN-defects are reported to be photo-stable, free of blinking and bleaching, even at elevated operation temperatures as high as 800K[14,16]. Most importantly the emitter is stable in an hBN-monolayer, of only nanometer thickness, readily accessible for local nanoscale control and top-down fabrication. Despite the key advantages of photostability and accessibility, also the hBN-defect is still limited in brightness as a single-photon source, due to its intrinsic luminescence lifetime of several nanoseconds. The atomically thin hBN seems ideal for local enhancement by a plasmonic nanoantenna. To this end, one needs to optimize the coupling between the hBN-emitter and the nanoantenna by deterministic control of position, distance, orientation and resonance. A few attempts have been reported: Tran *et al.* relied on nanoantenna arrays[17] and Nguyen *et al.* used AFM to couple individual hBN-defects to gold nanospheres[18]. Both studies reported a slight decrease in radiative lifetime alongside a minor increase in absolute photon emission rates, however in both cases the crucial emitter-positioning accuracy, was a limiting factor[18,17]. Additionally, the experiments were performed

in static systems, with fixed positions, complicating the systematic study of emitter-nanostructure interactions.

Here we present a systematic spatially resolved study of the coupling of hBN-defect single-photon emitters to resonant optical nanoantennas, with nanometric position-control and optical resolution of 40nm. By nanosecond time-gating we separate the hBN-defect emission, to record lifetime interaction maps and quantify the interaction strength between emitter and antenna. Based on our findings we propose a nanoantenna-hBN-defect design, with an order-of-magnitude enhanced brightness, suitable for on-chip top-down fabricated configuration.

First, we analyzed the general optical properties of hBN-defect emitters (Figure 1). Thin (~5nm) hBN-flakes are exfoliated onto a quartz substrate. These pristine flakes show a relatively low defect-density of less than one luminescent site per 50x50 μm^2, moreover mainly located along the flakes' edges. As these areas are generally not well suited for antenna probe scanning, we opt for Argon plasma etching, followed by high temperature annealing, to induce optically stable hBN-defects across the entire flake[19]. A typical luminescence image of a treated hBN-flake is shown in Figure 1a. We observe a near-constant luminescence background, of approximately 30kcnts/s, across the entire flake, diffraction-limited emission sites distributed over the entire flake and pronounced emission along the flake's edges. While the former are mainly induced during plasma etching, the latter are predominantly native defects. The emission spectra of individual defects (Figure 1b) show large heterogeneity, covering a spectral range from 550 to 700nm with the mean emission wavelength for plasma-etching-induced luminescent sites centered around 620nm (Figure 1c), in agreement with previous reports[20,21]. The photo-luminescence decay of individual defects shows a single exponential decay of τ=3.5 ns (Figure 1d), in line with previously reported values of a few nanoseconds[14,15]. To verify the single-photon-emitter nature of the hBN-defects, we record the second-order autocorrelation function. Around 5% of the measured hBN-defects does exhibit a dip below 0.5 at zero time delay, confirming single-photon emission, while the majority of the defects do not exhibit single-photon emission character[19]. A typical anti-bunching curve is shown in Figure 1e, exhibiting a $g^{(2)}(0)$ value of 0.4. This relatively high $g^{(2)}(0)$ value is due to the fact that roughly 20% of the collected photons comes from bulk emission of the hBN-flake. Finally, we determine the dipole orientation of the emission sites by

recording the luminescence response on the orientation of incident polarization (Figure 1f). The observed degree of polarization (DOP), computed as $(I_{max}-I_{min})/(I_{max}+I_{min})$, varies broadly from 0.1 to 0.9, without any preferred orientation with respect to the hBN-lattice[22]. The occurrence of near-isotropic excitation probabilities agrees with the low fraction of single-photon emitting-defects, suggesting the presence of multiple emitters inside a typical 300nm confocal spot of our microscope. The density of closely packed hBN-defects probably depends on the plasma etching conditions, used to increase the number of emitters in the exfoliated hBN-flakes (Methods).

Next, we turn to controlled nanoscale coupling of the hBN-defect emitter to a nanoantenna. To this end, we employ a scanning probe microscope (Methods), which allows to scan a nanofabricated antenna over a single-photon emitter, at a constant distance using shear-force distance controll[21]. Figures 2a and 2b show SEM images of the aluminum-nanoantennas probes employed in this study, fabricated onto the apex of a heat-pulled optical fiber by focused-ion-beam milling (Methods)[13,23]. A 160nm length of the 50x50nm cross-section Al antenna is fabricated, to be resonant with excitation or hBN-emission.

The Al nanoantenna does show weak single-photon luminescence. Therefore, we compared representative hBN-defect luminescence to the antenna signal. Typically a fluence of 40 kW/cm^2 is used, which is one order-of-magnitude below the fluences typically used to excite hBN-defects[14,18], and prevents thermal damage of the nanoantenna. Figures 2c and 2d show confocal luminescence images of an isolated hBN-defect as well as the dipolar Al-nanoantenna, excited with circular polarization, while the antenna is kept about 20nm from a clean quartz cover glass. Surprisingly, the weak antenna-emission is still two times brighter than the hBN-defect. In fact, the hBN-emission is very weak, which represents a considerable challenge for the antenna coupling experiments, as the respective signals have to be separated. An obvious solution would be to employ spectrally selective detection; however the respective emission spectra exhibit considerable overlap (Figure 2e). Moreover, the intrinsic hBN-emission-heterogeneity (Figure 1b,c) complicates spectral filtering for enhancing the signal-contrast as different detection filters would be necessary for each defect.

As an alternative to distinguish hBN and antenna, we employ time-gating of the collected luminescence signal. A comparison of the luminescence time-traces (Figure 2f) shows a rapid

decay, with <200ps lifetime, of the antenna luminescence. After 2ns the antenna-signal has essentially decayed to zero, while the hBN-signal has gone down only half. Thus, time-gating allows hBN-defect specific detection, in a post-processing manner, using time-correlated single-photon-counting detection (Methods).

After characterization of hBN and antenna emission, we now turn towards antenna scanning experiments to acquire interaction maps on the nanoscale. Figure 3a indicates schematically the experiment. First, we position the hBN-defect of interest in the center of our confocal excitation spot. Once positioned, we raster-scan the antenna probe in close proximity across the emission site, while keeping illumination and sample geometry constant, and detect the photon-emission as a function of the antenna position.

Figure 3b displays a near-field luminescence map with the antenna probe in close proximity to the hBN-defect. Here, we use the flat-dipolar Al nanoantenna (Figure 2a) fabricated with 160nm length for spectral resonance at 620nm, i.e. resonant with the excitation laser. Figure 3b shows a bright spot, approximately 300nm in diameter, with two darker spots superimposed, slightly offset to the top right of the image, due to non-perfect alignment of the hBN-defect within the confocal illumination spot. The 300nm spot is due to the antenna-luminescence, which is confirmed by the fact that for a retracted antenna one observes constant, uniformly distributed, hBN-defect photon-emission, irrespective of the antenna-position, as shown in Figure 3d. The two darker spots are indicative of antenna hotspots, localized at the apexes of the antenna, where coupling is maximized. To quantify the analysis, we exploit the previously mentioned time-gating to separate the fast antenna luminescence (<2ns) from the slower hBN emission. We detect all photons in a time-tagged fashion, which allows the generation of arrival-time filtered images during post-acquisition analysis[24]. Figure 3c shows the result of the time-gating analysis with the luminescence separated into two time-windows: 0-2 ns and 2-25 ns intervals. The first image contains mainly antenna as well as some hBN-defect contributions and therefore strongly resembles the initial interaction-map presented in Figure 3b. The second image, however, almost exclusively contains hBN-defect luminescence, exhibiting a markedly enhanced double-spot contrast, while the antenna luminescence spot is almost fully suppressed leaving a near-constant background across the entire image. Figure 3e further quantifies the effect of the 2ns time-gating with 2-fold contrast-improvement. The hBN-defect luminescence shows two depletion spots of

60nm, with maximum depletion approximately 75%, and separated by 150nm, in agreement with the aluminum antenna length of 160nm. We remark that these hotspot features are typical for either vertical or isotropic oriented emitters coupling to flat dipolar antennas as previously shown[23].

Time-gating the hBN-signal (>2ns) facilitates the extraction of quantitative lifetimes under varying coupling-conditions, thus allowing generation of a full interaction lifetime map, as shown in Figure 3f. Here, the uncoupled hBN-defect exhibits a lifetime of about 3.5ns, in agreement with the value presented previously (Figure 1d). Once entering a hotspot the lifetime decreases to approximately 1.6ns, i.e. a reduction of 2.2 times (Figure 3g).

These observations are somewhat surprising, as the observed local antenna-defect coupling and lifetime reduction does not result in the anticipated luminescence enhancement. To concentrate the antenna-field further and allow a smaller separation between antenna-apex and hBN-defect, we performed the experiment presented above with a 30° tilted dipolar antenna probe, which is excited out-of-resonance at 520nm wavelength (Methods). The chosen tilted antenna configuration allows a tighter spatial light-confinement compared to the previously employed flat antenna probe, thus providing higher resolution of the hBN-emission center and better coupling efficiency. Indeed, using the tilted antenna, we observe a single interaction-spot exhibiting a full-width half-maximum of only 45nm (Figure 4a, b). The improved interaction-strength and light confinement of the tilted antenna-probe results in even more reduction in antenna-luminescence. The antenna luminescence is slightly decreased with respect to the hBN-defect emission, as the antenna is excited out-of-resonance, yet the tilted antenna is unable to increase the hBN-emission-intensity beyond its free-space level.

As such, both the flat-dipolar as well as the tilted-dipolar antenna experiments presented in Figure 3 and 4, indicate that the antenna-hBN-defect interaction exclusively results in an overall emission depletion.

We have performed finite-difference time-domain (FDTD) simulations to explain our observations results. Figure 5 presents an overview of the simulation results for the flat dipole antenna. The calculation-geometry is outlined in Figure 5a. Here, the hBN-defect is located inside the hBN-flake, at a depth of 5nm, while the antenna is located at a distance of 20nm

from the hBN-surface, unless stated otherwise. The long resonant nanoantenna-axis is aligned with the x-direction. The calculated total electric field intensity in the vicinity of the antenna is shown in Figure 5b. Close to the surface, we observe an approximately 100-fold intensity increase, with respect to the incoming field. However, due to the high refractive index of hBN (n=2.2) as well as the high radius of antenna-curvature of 25nm the intensity enhancement inside the hBN-flake is only slightly above unity[25]. As a consequence, the antenna-induced excitation enhancement is approximately unity and, hence, negligible.

Figure 5c compares the calculated radiative and non-radiative rates, alongside the luminescence lifetime, for three different emission-dipole moment orientations. We concentrated on x-, z- and isotropic-oriented emitters. We omitted the y-oriented case since it exhibits a characteristic 4-lobe pattern[23] which we did not observe in our measurements. We decided to include the isotropic case might, as only 5% of all characterized hBN-defects showed anti-bunching, while the majority exhibited a very low DOP, suggesting that a large fraction of the hBN-defect emitters is composed of more than a single emitter. For all 3 cases, we observe a rate increase near the apex of the nanoantenna, both for the radiative as well as the non-radiative contribution, as expected for a resonant dipole-antenna. Assuming a luminescence lifetime of 3.5 ns, the reduction is plotted in Figure 5c. A direct comparison with the experimentally observed lifetimes (Figure 3f) reveals a quantitatively good agreement, with lifetime-minima separated by approximately 150nm. Yet assigning an emission-dipole orientation based on the results presented is rather difficult.

To further understand our observations we simulated the emission quantum efficiency (QE) of the emitters, where we assume unity QE for uncoupled defects, based on previously reported literature values[27,28]. As a result, upon interaction with the nanoantenna, the QE cannot be improved by enhanced radiative rate and can only be reduced by enhanced non-radiative rate (Figure 5c). Figure 5d reports the resulting QE values for the nanoantenna located 25nm, 15nm and 3nm above the hBN-surface, again for x-,z- and isotropic-oriented emitters. Indeed, QE depends strongly on the antenna-emitter configuration. At a distance of 25nm, we observe predominantly radiative decay with limited losses, but already at a distance of 15nm, the non-radiative rate becomes non-negligible and at 3nm we observe pronounced quenching with the QE reaching values below 10%.

Based on the simulations presented in Figure 5c and 5d we re-examine the experimental results (Figure 3). Firstly, the observed lifetime reduction shows quantitatively good agreement with the lifetime-simulations and does confirm considerable hBN-defect-antenna coupling. The simulations indicate that the excitation enhancement is strongly screened-off, due to the high refractive index of hBN, therefore we concentrate our analysis on the emission intensities (Figure 5d). In silico, x-oriented emitters exhibit emission profiles with a minimum at the center of the antenna, which fails to reproduce our experimental double-spot observations. Instead, z- and isotropic-oriented emitters do show two local minima, exhibiting a QE decrease of 30% and 20%, respectively. The measured emission depletion is 50% to 75%, depending on the time-gating. The antenna is modelled as a perfectly smooth, single crystalline, metallic object. In reality, SEM images and optical measurements show that, depending on fabrication conditions, a typical Al antenna is polycrystalline with 20-40nm size grains[29] which can explain the differences in emission-quenching.

Overall, the simulations suggest that, the hBN-emitter is either z- or isotropic-oriented as we observe a double-lobe pattern rather than a central spot, as expected for an x-oriented dipole. Based on these observations we conclude that the hBN-defect must be isotropically oriented as the z-orientation is unlikely given the in-plane excitation polarization. In other words, the hBN-emission center measured in Figure 3 is most likely composed of more than a single emitter, all of which randomly oriented, thus forming an average isotropic emission-center.

The overall picture suggests that, in this specific configuration, luminescence cannot be enhanced by manipulating the emission properties. First, internal QE of the hBN-emitters is already near-unity. Second, the excitation enhancement is not sufficient to compensate for the antenna losses, which is a direct result of the high refractive index of hBN and the large index step to the air-gap between defect and antenna. As a result, the interaction between antenna and hBN-defect leads to an overall emission-depletion, resulting in the observed dark spots at the antenna-apexes.

An important insight from our scanning antenna results is the fact that one needs to avoid the low index air gap to gain hBN-defect emission enhancement by antenna interaction. An alternative configuration is sketched in Figure 6a. Here, the aluminum antenna is fabricated directly on exfoliated hBN. Such configuration can be realized fabricating the nanoantennas directly on the hBN-layer by e-beam lithography, while the hBN-defect in close proximity

might be induced by gallium FIB exposure, as reported recently in the literature[30]. The nanoantenna directly on the hBN-flake, with sharp metal-hBN transition, results in a local field intensity enhancement of two orders of magnitude inside the hBN-layer (Figure 6b). The strong excitation enhancement can compensate for the decrease of QE due to antenna losses. FDTD simulations of the total excitation-emission enhancement, for an X and isotropic oriented hBN-defect emitter embedded inside a 5nm thick hBN-layer at 5nm lateral distance from the antenna, show, respectively, 15x and 10x total enhancement of photon emission. The presented configuration design in Figure 6 enables an order of magnitude higher luminescence emission, i.e. a brighter single-photon source. Importantly, the local excitation enhancement at the defect, will make the defect emission dominate over the intrinsic antenna luminescence, allowing direct hBN photon emission detection, without the need of time-gating.

To summarize, we presented, for the first time, the experimental near-field coupling of a hBN-defect emitter to a tailor-made resonant plasmonic nanoantenna, which we systematically scanned through the hBN-defect near-field, to generate a nanoscale interaction map. We employed dipolar nanorod antennas, both in planar and tilted geometry. The latter revealed single-hotspot images with 45nm FWHM, indicating that individual hBN-emission sites are confined to an area in size smaller than few tenths of nanometers.

We quantified both the antenna-position dependent luminescence intensity as well as the luminescence lifetime and, furthermore, implemented a time-gating strategy to separate the defect emission from the considerable intrinsic nanoantenna luminescence. Our data show that by relying on a resonant antenna configuration and the aforementioned time-gating it is possible to localize hBN-emission centers with nanometric accuracy within a 75% depletion dip while, simultaneously, shortening the lifetime by a factor of 2.2.

The anticipated antenna enhancement was not observed, in our near-field coupling experiments. The presented FDTD modelling suggests that emission enhancement is indeed difficult to achieve. This manifestation is due both to the non-coupled QE being close to unity and the fact that the high index hBN-layer serves as a screening layer, shielding the defect of the enhanced field in the vicinity of the nanoantenna. The latter point has important implications for plasmonic-coupling to solid-state emitters in general. Even though they are promising candidates for single-photon sources their small cross-sections and resulting small

emission rates calls for efficient enhancement strategies to ensure competitive performance when compared to other promising alternatives such as single molecules. Here, plasmonic cavities might, at first, seem like a valid strategy but the large refractive index of typical materials such as TMDCs, silicon or diamond prevents efficient electric field concentration. As such, it is necessary to reduce the materials' thickness to a minimum and to deterministically place the plasmonic antenna at a defined distance thus balancing excitation enhancement and quenching effects. At first, these constraints might appear prohibitive but the recent advances in nanofabrication based on He-based focused-ion-beam-milling and TMDC-manipulation put assembling such a coupled system within reach. Given that it is now possible to deterministically induce hBN-defects at well-defined positions within an hBN-layer[30,31] we propose a top-down fabricated on-chip single-photon source, based on hBN-defects coupled to plasmonic nanoantennas, that allows an absolute luminescence enhancement of 10 to 15-fold, thus providing a one order-of-magnitude brighter single-photon source, with no need for time-gating detection.

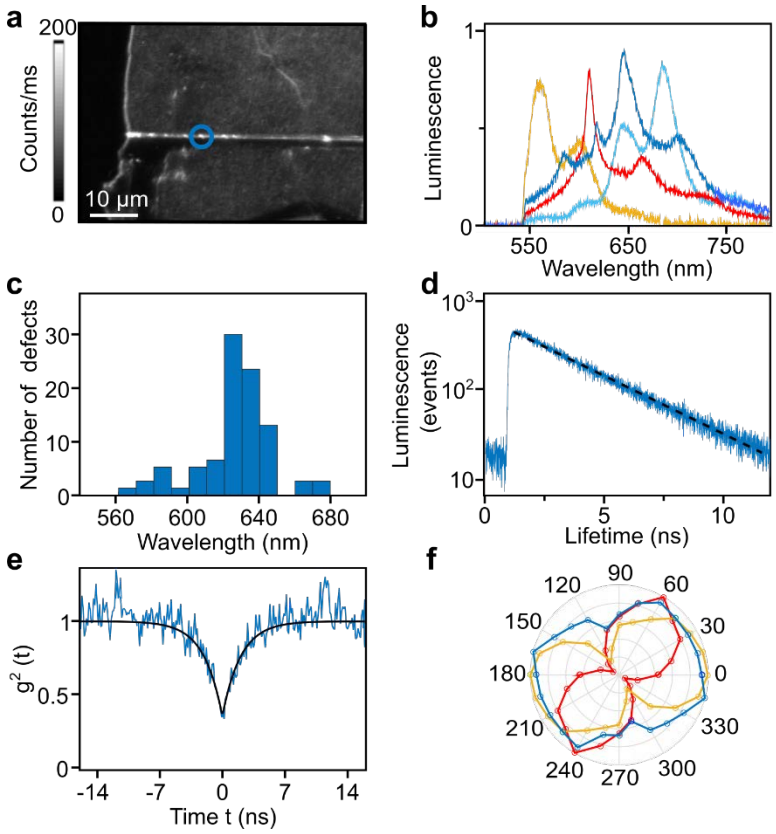

Figure 1. Optical properties of hBN-defect emitters. (a) Confocal luminescence image of an exfoliated hBN flake. The majority of the emitters is located at the edges of the flake, while a few, oxygen-plasma induced, defect are present on the flake area itself. (b) Representative emission spectra of various hBN-defects. (c) Histogram of the spectral emission maxima of a total of 95 hBN defects. (d) Typical luminescence decay (blue) and single-exponential fit (red, dashed) with a lifetime of 3.5 ns. (e) Second-order-correlation time response (blue) of the defect highlighted in (a) showing anti-bunching, and exponential fit with 3.5 ns lifetime (red). (f) Representative excitation polarization dependence of three different hBN emission sites with degrees of polarization of 0.1, 0.67 and 0.9.

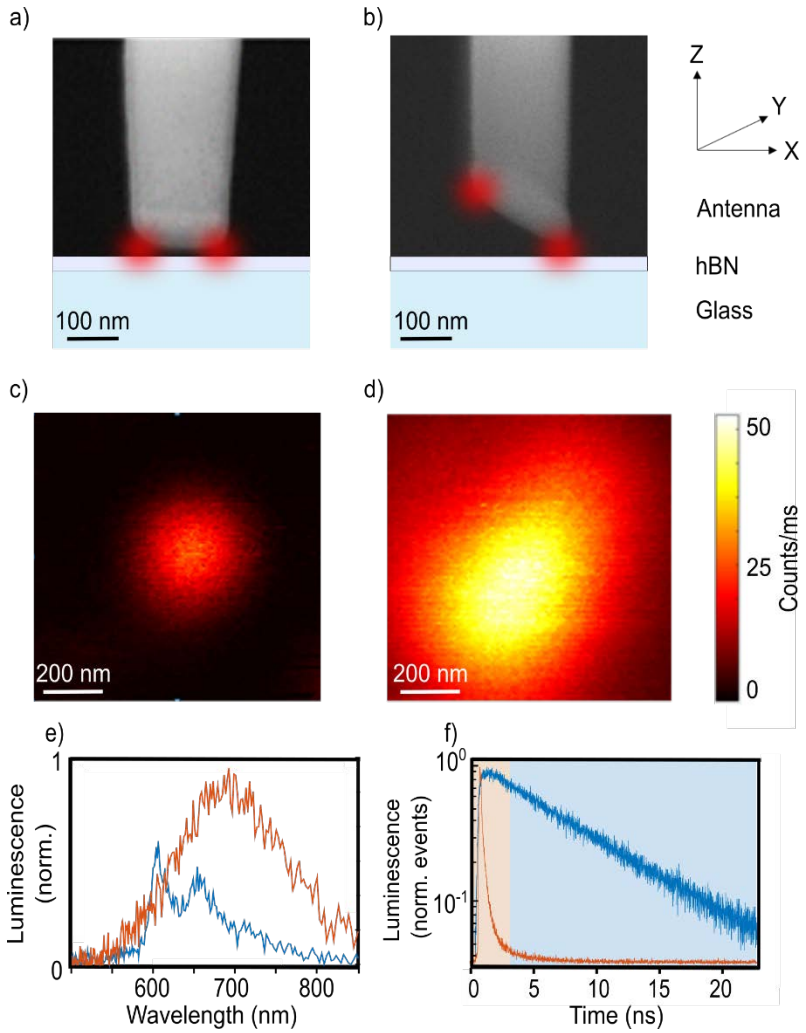

Figure 2. Luminescence of hBN-defect and nanoantenna. (a, b) SEM images of an aluminum nanoantenna probe, either a flat (a) or a 30° tilted (b) rod antenna, supported on glass. The dipolar antenna has hotspots on either side (red), which couple to the hBN-defect (blue). (c) Confocal luminescence image of a hBN-defect and (d) of the dipolar antenna shown in (a), positioned in close proximity of a clean quartz cover glass, both plotted on the same intensity-scale. (e) Luminescence spectra on same scale of both hBN-defect (blue) and antenna (orange). (f) Photon-arrival histograms for the hBN defect (blue) and the nanoantenna emission (orange).

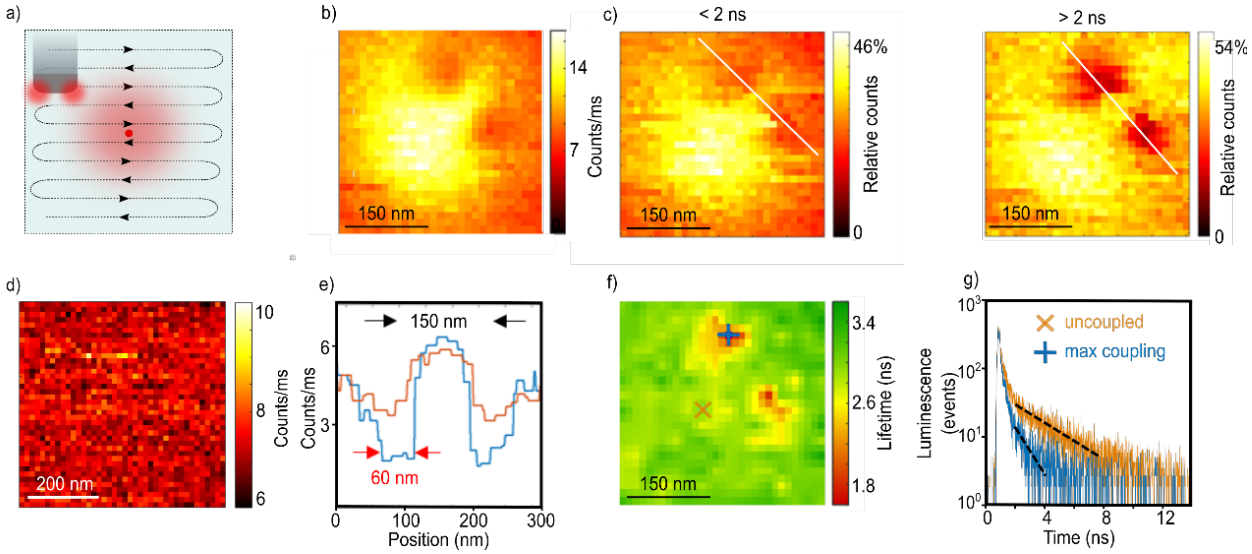

Figure 3. Nanoantenna mapping of individual hBN emission centers. (a) Schematic of a typical antenna probe scan over a continuously illuminated emitter. (b) Near-field image of an hBN defect using the flat dipolar antenna. (c) Time gated luminescence maps using time intervals of 0-2 ns (left) and 2-25 ns (right). (d) Near-field image of an hBN-defect, with the dipolar antenna probe retracted. (e) Line profiles along the paths indicated in (c) for intervals 0-2ns (orange) and 2-25ns (blue). (f) Fluorescence lifetime-map obtained by fitting the 2-25 ns time-interval to a single exponential decay. (g) Photon-arrival histograms for the two points indicated in (f) alongside single-exponential fits (black dashed) indicating coupling-induced lifetime reduction.

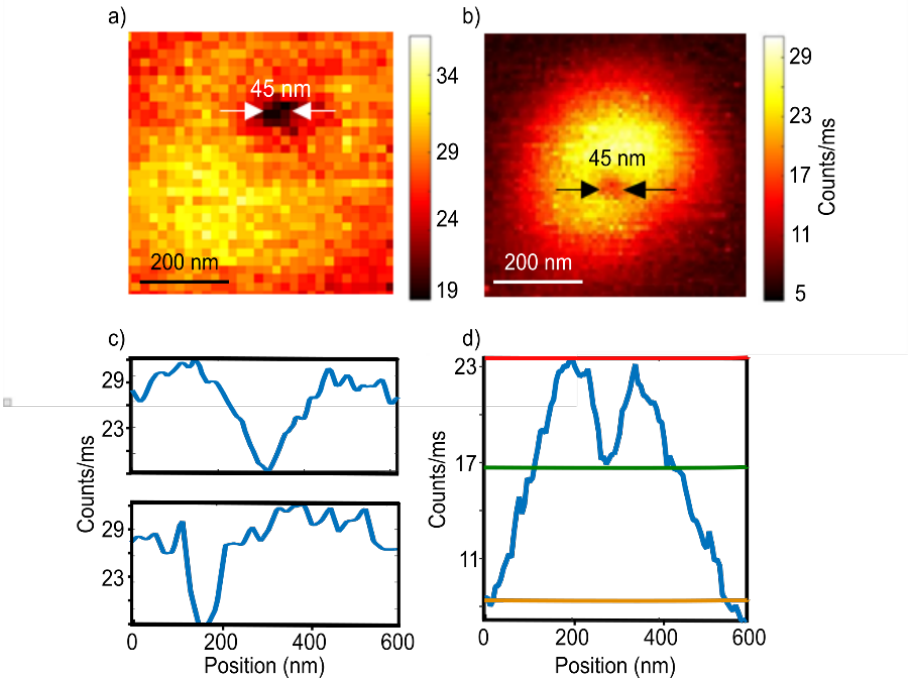

Figure 4. Imaging with a tilted dipolar antenna. (a) Probe scan image of an hBN emission center with the tilted dipolar antenna shown in Figure 2b. (b) Confocal fluorescence image of the same hBN defect with the antenna being positioned above it, the emitter is localized with a 45 nm size depleted spot. (c) Horizontal (top) and vertical (bottom) profiles obtained from the antenna-scan. (e) Horizontal profile of the confocal image.

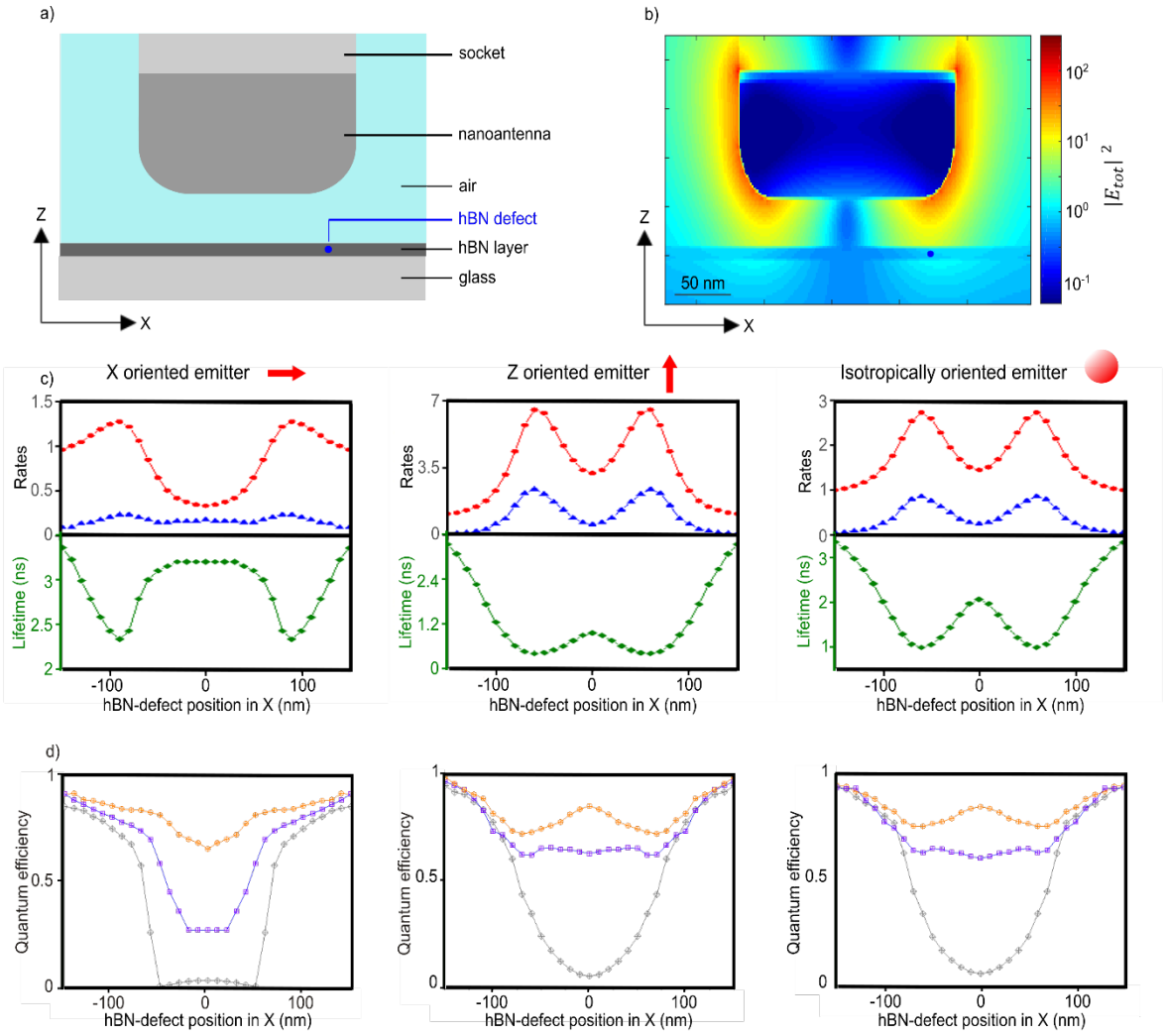

Figure 5. FDTD simulations of the excitation and emission properties of an hBN-defect located in close proximity to a dipolar nanoantenna. (a) Sketch of the typical antenna-hBN-defect emitter configuration. The plotted aspect ratio is elongated by a factor of two in the z-dimension, for the sake of clarity. (b) Electric field intensity map across the antenna when driven by a plane wave with a wavelength of 620 nm.(c) Radiative rates (red) and non-radiative rates (blue), relative to uncoupled emitter, as well as the luminescence (green), at an antenna to defect distance of 25 nm, for x-oriented (left), z-oriented (center) and isotropic-oriented emitters (right). (d) Quantum efficiency of hBN emitters located at different z-distances of 25 nm (orange), 15 nm (purple) and 3 nm (grey) for x-oriented (left), z-oriented (center) and isotropic-oriented emitters (right).

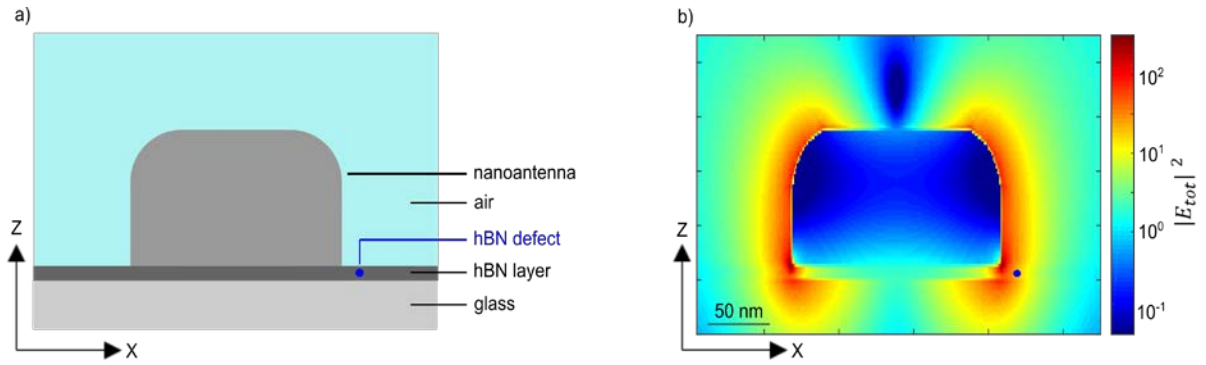

Figure 6. FDTD simulation of the excitation of an hBN defect in close proximity to a dipolar nanoantenna without air gap. (a) Sketch of a dipolar nanoantenna directly on top of a 5 nm thick hBN layer. The hBN emitter is located inside the hBN layer at a lateral distance of 5 nm from the antenna. (b) x-z map of the electric field intensity around the structure shown in (a) excited at a wavelength of 620 nm. The hBN-defectis indicated by the blue dot.

METHODS

Preparation of hBN Defects. hBN flakes are exfoliated directly with Scotch tape on top of quartz substrate, or dry transferred on top of pre-patterned nano-antennas following a dry transfer method. The dry transfer involves the exfoliation of hBN flakes on polydimethylsiloxane (PDMS) stamps, and a subsequent transfer onto the target substrate with the antennas. The use of quartz allows high temperature treatment of the materials and provides a one order of magnitude lower fluorescence background compared to normal glass coverslips. To induce defects into the hBN flakes, the samples are exposed to Oxygen and Argon plasma etching (with respectively 150 and 80 W power for 2 minutes).[19] The samples are then thermally treated for 30 minutes at 850 °C in Argon atmosphere to stabilize the defects. Overall this process provides thin hBN flakes (<10 nm) with a high density of stable hBN emitters.[16,30]

Antenna preparation. The antenna material, size and aspect ratio are designed in order to act as $\lambda/2$ dipole nanoantennnas, with a tunable resonance. The antennas are fabricated at the apex of a tapered optical fiber. The fiber is used as a support for the antenna, which is scanned in close proximity of the sample surface allowing the near-field interaction with the emitters. The antenna is fabricated out of a thin layer of aluminum deposited at the apex of the fiber, by means of Ga^{+} focused-ion-beam-milling (FIB). This reliable and reproducible method allows the fabrication of nanoantennas as scanning probes with a specific 3D orientation. The antennas are fabricated with a length of 160 nm and lateral size of 50x50 nm^2 with resonance at 620 nm wavelength. The orientation is flat or tilted of 30° with respect to the horizontal plane. A detailed description of the flat antennas fabrication procedure can be found in reference.[23]

Scanning Antenna Microscope. The experiments were performed with a custom-built near-field microscope. It consists of an inverted confocal microscope, with a scanning probe head. The system allows the independent scanning of both the probe and the sample by means of a shear-force feedback mechanism. It allows keeping the probe at a constant distance of approximately 10-20 nm from the sample surface. This way the near-field coupling between the antenna and the emitter located in the hBN flake is permitted, with nanometer precision.

Two main scanning configurations are possible: the probe can be scanned over an emitter continuously illuminated inside the diffraction-limited spot, or the sample can be scanned with the probe located in close proximity of the surface centered on the diffraction-limited spot.

The emitters are illuminated with light of 520 and 620 nm wavelength, focused using a 100x 1.3 NA oil immersion objective. Since the actual orientation of the antenna at the end of the probe is unknown, the system is excite with circular polarization. The laser power before the objective is 150 μW for the measurements in Figure 1 and 20 μW for all the other measurements, in order to prevent the melting of the antenna. Those values correspond respectively to energy densities of 300 and 40 kW/cm^2. Under these conditions, the hBN defects remained active for several months.

In collection path, long pass filters are used in order to separate the reflected excitation light. The fluorescence is confocally imaged onto two fast avalanche photodiodes (APD) (PD-050-C0D, Micro Photon Devices) for single-photon counting and photon correlation. The collected light can also be sent to a custom-built spectrometer. In the spectrum is detected by means of an electron-multiplying charge-coupled device (EM-CCD) (Image EM x2 EM-CCD Camera C9-100-23B, Hamamatsu). The spectra integration time in figures 1b and 2e is 200 ms.

Photon Time-Gating Imaging and Lifetime Maps. The hBN defects are excited with a picosecond pulsed tunable laser (λ= 520 or 620 nm, pulse width ~70 and 30 ps respectively, SuperK Extreme, NKT Photonics), with 80 MHz repetition rate for data showed in figure 1 and 40 MHz for all the other cases. The use of time-correlated single-photon counting (TCSPC) correlator (PicoHarp 300, PicoQuant GmbH) allows the recording of the absolute arrival time of the emitted photons on the APDs, with respect to the excitation pulse with 8 ps resolution. The instrument response function is of ~200 ps full-width half-maximum for light of a wavelength of 520 nm. Customized software allows the synchronization of this equipment with the scanning antenna microscope, in order to obtain intensity maps with photons histograms recorded at every pixel.

With subsequent data analysis it is possible to obtain intensity images integrating the photons at every pixel in specific time ranges, hence producing time-gated images, as shown in Figure 3 (b) and (c). Since the luminescence of the antenna is limited only to the first 2 ns, this

technique allows the separation of the photons emitted by the metallic antenna and the hBN defect. Once that the emitter photons have been isolated by time-gating, a single exponential fit of the photons histograms at every pixel allows the generation of lifetime maps, as shown in Figure 3 (a).

Second-Order Cross-Correlation Measurements. We use a Hanbury-Brown-Twiss setup for second-order photon autocorrelation. The signal is split 50/50 on to two APDs both with a time response of 200 ps at a wavelength of 520 nm. The photon arrival times on the APDs are cross-correlated, revealing the photon second-order autocorrelation of the hBN defects, and proving their single-photon emission behavior, as shown in Figure 1 (e). The correlation histograms are recorded with a bin size of 8 ps and later binned at 64 ps.

Numerical Simulations. We solve Maxwell's equations using a finite-difference time domain (FDTD) commercial solver (Lumerical Solutions, Inc., Vancouver). In general the hBN layer has been modeled as a 5 nm thick material with a refractive index n=2.2.[25,26] The dipolar antenna has been modeled as an aluminum nanorod of 160 or 140x50x50 nm.

In order to quantify the excitation enhancement in Figure 5(b) and 6 (b), the total electric field intensity $|E_{tot}|^2$ across the antenna and the hBN layer has been calculated by FDTD. The given values have been normalized to the incoming total electric field intensity $|E_{inc}|^2$. Both, the excitation field and the one scattered by the antenna are simulated.

In Figure 5 (b) the source has been modeled as a circularly polarized one. In Figure 6 (b) the source has been modeled as a linearly polarized one, because the orientation of the antenna in X-Y plane would be known by fabrication and the polarization of the excitation beam might be easily aligned with it.

In Figure 5(b) the antenna is modeled as an aluminum nanorod of 160x50x50 nm, located 20 nm from the hBN layer. In Figure 6 (b) the antenna is located directly on a 5 nm thick hBN layer. This red shifts the resonance, and in order to have a dipolar antenna resonant at 620 nm, its length has been reduced to a size of 140x50x50 nm.

For the simulations of rates and lifetime profiles presented in Figure 5the antenna has been located at 20 nm from the hBN layer. The emitter is simulated as a dipole emitter with internal quantum efficiency $\eta = 1$ and it is located inside the hBN layer, below the antenna. The

emitter is modeled as a dipole oriented in X, Z and approximately isotropic. The latter emitter has been obtained combining the emission of three perpendicularly oriented emitters.

For the lifetime profiles the total power radiated by the emitter alone and the one of the emitter located in every specific configuration with respect to the antenna are compared. The ratio between the two powers is the reduction of lifetime at each antenna-emitter position.

The radiative and non-radiative rates shown in figure 5 are simulated in a similar way, taking into account that the light absorbed by the metallic antenna constitutes the non-radiative rate, while the light radiated in the far-field represents the radiative one.

The QEs reported in Figure 5 have been obtained placing the emitters at 25, 15 and 3 nm distance from the antenna. The values have been obtained with the following relation $QE = \frac{\eta_{\mathrm{rad}}}{\eta_{\mathrm{rad}}+\eta_{\mathrm{non-rad}}}$, where η_{rad} and $\eta_{\mathrm{non-rad}}$ are respectively the radiative and non-radiative rates.

Acknowledgements

N.F.v.H. acknowledges the financial support by the European Commission through ERC Advanced Grant 670949-LightNet. D.K.E. acknowledges support the H2020 Programme under grant agreement n° 820378, Project: 2D SIPC and the La Caixa Foundation. Authors acknowledge support by the Ministry of Science, Innovation & Universities (RTI2018-099957-J-I00 and PGC2018-096875-B-I00), the Ministry of Economy (FIS2015-69258-P, BES-2016-078727 and “Severo Ochoa” program for Centers of Excellence in R&D SEV-2015-0522), the Catalan AGAUR (2017SGR1369), Fundació Privada Cellex, Fundació Privada Mir-Puig, and Generalitat de Catalunya through the CERCA program. We thank Kevin Schädler for help in initial phase of hBN sample fabrication.

Author contributions:

N.P.B., M.L. and N.F.v.H. designed the experiment. N.P.B. fabricated nanoantenna probes, performed the experiments, analyzed the data and performed numerical modelling. T.T. and K.W. provided hBN. X.L. and D.K.E. exfoliated hBN flakes. N.P.B., M.L., D.K.E. and N.F.v.H. wrote the manuscript.

The authors declare no competing financial interest

References

1. Aspuru-Guzik, A. Photonic quantum simulators. *Nat. Phys.* **8**, 285–291 (2012).
2. Lo, H. Secure quantum key distribution. *Nat. Photonics* **8**, 595–604 (2014).
3. Reimer, M. Bright single-photon sources in bottom-up tailored nanowires. *Nat. Commun.* **3**, 737 (2012).
4. Lounis, B. Single photons on demand from a single molecule at room temperature. *Nature* **407**, 491–493 (2000).
5. Lombardi, P. Photostable Molecules on Chip: Integrated Sources of Nonclassical Light. *ACS Photonics* **5**, 126–132 (2018).
6. Doherty, M. The nitrogen-vacancy colour centre in diamond. *Phys. Rep.* **528**, 1–45 (2013).
7. Hepp, C. Electronic structure of the silicon vacancy color center in diamond. *Phys. Rev. Lett.* **112**, 036405 (2014).
8. He, Y. *et al.* Single quantum emitters in monolayer semiconductors. *Nat. Nanotechnol.* **10**, 497–502 (2015).
9. Siampour, H. Chip-integrated plasmonic cavity-enhanced single nitrogen-vacancy center emission. *Nanoscale* **9**, 17902–17908 (2017).
10. Katsumi, R. Quantum-dot single-photon source on a CMOS silicon photonic chip integrated using transfer printing. *APL Photon.* **4**, 036105 (2019).
11. Toninelli, C. Near-infrared single-photons from aligned molecules in ultrathin crystalline films at room temperature. *Opt. Express* **18**, 6577 (2010).
12. Hoang, T. Ultrafast Room-Temperature Single Photon Emission from Quantum Dots Coupled to Plasmonic Nanocavities. *Nano Lett.* **16**, 270–275 (2016).
13. Singh, A. Nanoscale Mapping and Control of Antenna-Coupling Strength for Bright Single Photon Sources. *Nano Lett.* **18**, 2538–2544 (2018).
14. Tran, T. T. Quantum emission from hexagonal boron nitride monolayers. *Nat. Nanotechnol.* **11**, 37–41 (2016).
15. Martínez, L. J. Efficient single photon emission from a high-purity hexagonal boron nitride crystal. *Phys. Rev. B* **94**, 121405 (2016).
16. Kianinia, M. *et al.* Robust Solid-State Quantum System Operating at 800 K. *ACS Photonics* **4**, 768–773 (2017).
17. Tran, T. T. Deterministic Coupling of Quantum Emitters in 2D Materials to Plasmonic Nanocavity Arrays. *Nano Lett.* **17**, 2634–2639 (2017).
18. Nguyen, M. Nanoassembly of quantum emitters in hexagonal boron nitride and gold nanospheres. *Nanoscale* **10**, 2267 (2018).
19. Xu, Z. Single photon emission from plasma treated 2D hexagonal boron nitride. *Nanoscale* **10**, 7957–7965 (2018).
20. Tran, T. T. Robust Multicolor Single Photon Emission from Point Defects in Hexagonal Boron Nitride. *ACS Nano* **10**, 7331–7338 (2016).
21. Tawfik, S. First-principles investigation of quantum emission from hBN defects. *Nanoscale* **9**, 13575–13582 (2017).
22. Exarhos, A. Optical Signatures of Quantum Emitters in Suspended Hexagonal Boron Nitride.

ACS Nano **11**, 3328−3336 (2017).

23. Singh, A. Vectorial nanoscale mapping of optical antenna fields by single molecule dipoles. *Nano Lett.* **14**, 4715−4723 (2014).

24. Wahl, M. Dead-time optimized time-correlated photon counting instrument with synchronized, independent timing channels. *Rev. Sci. Instrum.* **78**, 033106 (2007).

25. Lee, S. Refractive Index Dispersion of Hexagonal Boron Nitride in the Visible and Near-Infrared. *Phys. Status Solidi B* **256**, 1800417 (2018).

26 Rah, Y. Optical analysis of the refractive index and birefringence of hexagonal boron nitride from the visible to near-infrared. *Optics Letters* **44**, 3797 (2019).

27. Schell, A. Quantum Emitters in Hexagonal Boron Nitride Have Spectrally Tunable Quantum Efficiency. *Adv. Mater.* **30**, 1704237 (2018).

28. Nikolay, N. Direct measurement of quantum efficiency of single-photon emitters in hexagonal boron nitride. *Optica* **6**, 1084–1088 (2019).

29. Albrecht, G. Comprehensive study of plasmonic materials in the visible and near-infrared: Linear, refractory, and nonlinear optical properties. *ACS Photonics* **5**, 1058–1067 (2018).

30. Ziegler, J. Deterministic Quantum Emitter Formation in Hexagonal Boron Nitride via Controlled Edge Creation. *Nano Lett.* **19**, 2121–2127 (2019).

31. Choi, S. Engineering and Localization of Quantum Emitters in Large Hexagonal Boron Nitride Layers. *ACS Appl. Mater. Interfaces* **8**, 29642–29648 (2016).